Research Square

Preprints are preliminary reports that have not undergone peer review.
They should not be considered conclusive, used to inform clinical practice,
or referenced by the media as validated information.

Basin sill depth and episodic flushing influence bathypelagic nekton communities and goose-beaked whale foraging in the Southern California Bight

Shannon Dolan

shdolan@ucsd.edu

Scripps Institution of Oceanography, University of California San Diego https://orcid.org/0009-0002-5701-7594

David Demer

NOAA Fisheries-Office of Science and Technology

Alba Solsona-Berga

Scripps Institution of Oceanography, University of California San Diego https://orcid.org/0000-0003-4096-742X

Clara Schoenbeck

Scripps Institution of Oceanography, University of California San Diego

Julie Dinasquet

Scripps Institution of Oceanography, University of California San Diego

Lauren Baggett

Scripps Institution of Oceanography, University of California San Diego

Ana Sirovic

Trondhjem Biological Station, Norwegian University of Science and Technology

Joseph Warren

Stony Brook University https://orcid.org/0000-0001-6920-1554

Sarah Gille

Scripps Institution of Oceanography, University of California San Diego

Simone Baumann-Pickering

University of California San Diego https://orcid.org/0000-0002-3428-3577

Article

Keywords: Ziphius cavirostris, acoustics, dissolved oxygen, environmental DNA, internal tides, water mass, ventilation

Posted Date: August 5th, 2026

DOI: https://doi.org/10.21203/rs.3.rs-10208495/v1

License: This work is licensed under a Creative Commons Attribution 4.0 International License.
Read Full License

Additional Declarations: There is **NO** Competing Interest.

Basin sill depth and episodic flushing influence bathypelagic nekton communities and goose-beaked whale foraging in the Southern California Bight

Shannon M. Dolan[1,*], David A. Demer[2]
Alba Solsona-Berga[1], Clara M. Schoenbeck[1]
Julie Dinasquet[1], Lauren M. Baggett[1], Ana Širović[3]
Joseph D. Warren[4], Sarah T. Gille[1], Simone Baumann-Pickering[1]

[1] Scripps Institution of Oceanography, University of California San Diego, La Jolla, CA 92037, USA
[2] NOAA Fisheries-Office of Science and Technology, Silver Spring, MD, USA
[3] Trondhjem Biological Station, Norwegian University of Science and Technology, Trondheim, Norway
[4] School of Marine and Atmospheric Sciences, Stony Brook University, Southampton, NY, USA
[*] Corresponding author: shdolan@ucsd.edu

Abstract

Basin-scale (5–50 km) hydrographic variability within the Southern California Bight (SCB) structures bathypelagic (>1000 m depth) mid-trophic nekton communities and the prey community available to deep-diving predators such as goose-beaked whale. At three mooring sites, we combine multi-year time series of hydrography, acoustic backscatter, and passive acoustics with environmental DNA (eDNA) from conductivity-temperature-depth (CTD) casts to resolve fine-scale spatiotemporal variability (h–seasons) in water mass composition, bathypelagic nekton distribution, and beaked whale echolocation clicks at ∼1200 m depth. Despite narrow temperature (<0.67°C) and salinity (<0.056 g kg^{-1}) ranges, persistent differences between basin hydrography corresponded with distinct nekton assemblages: acoustic backscatter composition and cephalopod eDNA composition both indicated site-specific communities differentiated by dissolved oxygen (DO). Internal waves redistributed existing nekton patches at tidal timescales, while larger-scale physical forcings modulated total nekton backscatter over seasonal to interannual periods. In one case, an episodic basin flushing event coincided with increased nekton backscatter and a subsequent increase in goose-beaked whale acoustic detections. Collectively, these findings suggest that the SCB is a mosaic of heterogeneous bathypelagic habitats, with basin bathymetry and frequency of deep-water exchange jointly determining mid-trophic nekton community structure.

Keywords: *Ziphius cavirostris*; acoustics; dissolved oxygen; environmental DNA; internal tides; water mass; ventilation

Goose-beaked whales (*Ziphius cavirostris*; hereafter *Z. cavirostris*) regularly dive below 1000 m depth to echolocate and forage on bathypelagic nekton, primarily cephalopods, as well as mesopelagic fishes and crustaceans [1, 2, 3]. *Z. cavirostris* are present year-round in the Southern California Bight (SCB) with peak abundance shifting among basins, particularly near San Clemente Island and the Channel Islands [4, 5]. Because the densities of bathypelagic prey are low relative to the energetic demands of large predators, beaked whales must locate aggregations of nekton [6, 7]. The physical drivers shaping the spatiotemporal distribution of bathypelagic nekton in the SCB remain poorly understood [8].

The SCB is shaped by oceanographic processes spanning a wide range of temporal and spatial scales [9, 10, 11, 12]. These include wind-driven upwelling [13], mesoscale and submesoscale eddies [14], internal tides and waves [15, 16], and basin-scale circulation [17], all of which collectively structure the three-dimensional distribution of water masses [18]. Basin sill depths further regulate water mass exchange and retention, including episodic flushing events, or rapid intrusions of colder, more oxygenated water into basin interiors [19, 20, 21]. These hydrographic processes shape benthic biological community structure [22, 23], yet their influence on bathypelagic mid-trophic nekton aggregation and predator foraging remains poorly resolved.

At approximately 800–1200 m depth in the North Pacific, the four primary water masses include North Pacific Intermediate Water (NPIW), Antarctic Intermediate Water (AAIW), Upper Circumpolar Deep Water (UCDW) and Pacific Deep Water (PDW), each characterized by distinct temperature, salinity, and oxygen properties [24]. Variability in water masses is associated with shifts in microbial communities at the base of the food web [25], with potential cascading effects on mid-trophic nekton aggregations. In the SCB, changes in upper-ocean (<400 m depth) water masses during El Niño events and periods of increased Pacific Equatorial Waters have also been linked to increased *Z. cavirostris* presence [26], suggesting that hydrographic transitions may signal favorable foraging conditions at depth.

This predator–prey–environment system is further shaped by the diverse life-history strategies of both mid-trophic nekton [27] and their predators [28, 29, 30]. Bathypelagic cephalopods exhibit ontogenetic vertical migrations [31], semelparity [32], brooding behaviors [33], and diverse metabolic strategies [34, 35]. Mesopelagic fishes and crustaceans similarly exhibit complex reproductive and life-history strategies [36]. Superimposed on a physically dynamic and topographically constrained environment, these life-history traits generate patchy and transient nekton aggregations that highly mobile predators must locate and exploit within a complex four-dimensional environment [8, 37, 38].

Disentangling predator–nekton–environment processes requires simultaneous observations of predator presence, nekton distribution, and environmental variability at temporal and vertical resolutions sufficient to resolve ephemeral events. Particularly rare are coincident measurements of biological and physical signals at bathypelagic depths, with resolutions from h to months.

This study presents a multi-year, multi-instrument mooring dataset collected at three sites within the SCB (Fig. 1). The resulting Eulerian time series captures fine-scale nekton dynamics and concurrent environmental variability within *Z. cavirostris* habitat. Selected sites span contrasting basin bathymetries and hydrographic regimes (Fig. 1a,b). Site W, located west of the Santa Cruz Basin, is the deepest and most exposed to open-ocean conditions, with relatively deep sills facilitating exchange with offshore waters. Site E, within Tanner Basin, has moderate sill depths, with the California Current flowing along the basin's western boundary. Site H, located 40 km east of Site E within San Nicolas Basin, is a bowl-shaped basin with comparatively shallow sills that restrict water exchange.

Each mooring included sensors to measure acoustic backscatter, marine mammal vocalizations, and oceanographic conditions (Fig. 1c,d). A 70 kHz single-frequency Wideband Autonomous Transceiver (WBAT; Kongsberg Norway) echosounder measured nekton backscatter, interpreted as putative prey density. A hydrophone [39] recorded *Z. cavirostris* echolocation clicks, indicating their acoustic presence and presumed foraging [2]. A MicroCAT (SBE 37 ODO; Sea-Bird Scientific, Bellevue, WA) measured conservative temperature (Θ; °C), absolute salinity (S_A; g kg^{-1}), and DO, characterizing the concurrent hydrographic environment. Deployment dates and sampling periods for each instrument are provided in Table S1.

The objectives of this study are to: (1) quantify temporal variability in bathypelagic nekton backscatter across sites with contrasting bathymetric and hydrographic structure, (2) identify water mass properties associated with changes in nekton density and distribution, (3) evaluate whether recurring environmental forcings consistently coincide with nekton aggregations, and (4) examine how variability in mid-trophic nekton availability relates to the acoustic presence and presumed foraging activity of *Z. cavirostris*. By integrating multi-year passive acoustic, acoustic backscatter, and oceanographic observations, this study resolves fine-scale physical–biological dynamics and improves interpretation of bathypelagic processes.

Results

Multi-Scale Temporal Variability in Hydrography and Nekton Backscatter

Physical and biological conditions varied across overlapping temporal scales at all sites, from tidal to seasonal to interannual (Fig. 2; Extended Data Figs. 1, 2). Θ, S_A, potential density anomaly (σ_0; kg m^{-3}, calculated as $\sigma_0 = \rho(S_\mathrm{A}, \Theta, 0) - 1000$, where ρ is seawater density in kg m^{-3} referenced to surface pressure), and nekton backscatter (nautical area backscattering coefficient, s_A; m^2 nmi^{-2}, a measure of integrated acoustic backscatter from putative prey signals, proportional to their abundance and size) all exhibited tidal variability superimposed on seasonal and interannual fluctuations (Fig. 2, 4). At Site W, periods of warmer, fresher, and less dense water (for example, June 2023) coincided with reduced total nekton backscatter (Fig. 2). Daily-averaged σ_0 binned to 0.005 kg m^{-3} is overlaid to highlight longer-scale hydrographic variability (Fig. 2).

Even during extended periods of relatively stable hydrographic conditions, tidal oscillations in temperature, salinity, and nekton distribution remained evident at h timescales. Multiple physical processes interact with bathypelagic nekton on differing timescales.

Hydrographic Structure Shapes Nekton Assemblages Among Submarine Basins

Across sites, hydrographic conditions were constrained but distinct (Fig. 3a, b). In the combined dataset spanning all sites and a total of 38,191 h observations (1,591 sampling days), Θ varied by <0.67 °C and S_A by <0.056 g kg^{-1} (Table S2). Despite occasional overlap in σ_0 among sites, DO further differentiated sites (Fig. 3b).

Optimum Multiparameter (OMP) analysis indicated that all sites comprise mixtures of UCDW and AAIW, with the highest UCDW fraction at the deepest site (Site W; MicroCAT depth ∼1300 m; UCDW ∼60–70%), consistent with elevated S_A and DO relative to Sites E and H (Extended Data Fig. 3). Sites E and H, separated by approximately 40 km, exhibited similar Θ and S_A but differed in DO: Site H experienced persistent severe hypoxia (DO $\leq$ 0.5 mL L^{-1}) [40] throughout 2022–2023, whereas Site E consistently remained above this threshold over the same period.

During 2017–2018, however, DO at Site E approached severe hypoxia, reaching values comparable to those observed at Site H in 2022–2023. Since no concurrent measurements exist for Site H during 2017–2018, it is unknown whether hypoxia at Site H would have matched or exceeded conditions at Site E during that period. This interannual variability in DO around a biologically critical threshold suggests fluctuating conditions for bathypelagic biological communities at Site E.

These hydrographic differences corresponded with distinct communities as characterized by both tracks of individual nekton and eDNA. Distributions of median track target strength (TS; dB re 1 m^2, a measure of the acoustic backscattering cross-section of an individual organism) differed significantly among sites (Kruskal-Wallis test, $p < 0.001$; Fig. 3c): Site E exhibited the highest median TS (−51.3 dB re 1 m^2; IQR = 3.45 dB; n = 56,821) with a bimodal distribution, Site W intermediate values (−52.4 dB re 1 m^2; IQR = 1.82 dB; n = 181,292), and Site H the lowest (−53.1 dB re 1 m^2; IQR = 1.47 dB; n = 116,611). Pairwise differences among all sites were significant following Wilcoxon rank-sum tests with Benjamini-Hochberg correction (all adjusted $p < 0.001$).

Cephalopod eDNA from CTD-cast samples conducted in both spring and fall (>500 m depth) further resolved taxonomic differentiation among sites (Fig. 3d): Sites E and W were dominated by Gonatidae (72% and 74.1% of family-level detections, respectively), whereas Site H was characterized by a more diverse assemblage with prominent contributions from Histioteuthidae (33.1%) and Gonatidae (30.5%). The principal environmental distinction separating Site H from Sites E and W was persistently lower DO, suggesting that Histioteuthidae and associated taxa may be better adapted to severe hypoxic conditions.

Nekton Responses to Hydrographic Forcing Across Temporal Scales

Spectral analysis revealed elevated power in σ_0 at semidiurnal (S2, 12.000 h; M2, 12.421 h) and diurnal (K1, 23.934 h; O1, 25.819 h) tidal frequencies [41]. Backscatter (s_A) showed comparable periodicities, though with site-specific variability: Site H exhibited peaks at S2 and K1, Site W at S2, and Site E at O1. These patterns suggest that internal tides drive redistribution of bathypelagic nekton on tidal timescales within each basin (Fig. 4a). Across all sites, spectral power in both σ_0 and s_A increased toward monthly periods, consistent with the seasonal variability observed in the time series (Fig. 2).

Site-specific generalized additive models (GAMs) identified σ_0 as a significant predictor of s_A at Sites E and W, and DO at Site H (Fig. 4b). Additional model specifications and diagnostics are provided in Table S3. Along the σ_0 continuum, nekton backscatter increased with density across the lower range occupied by Site E ($R^2 = 0.202$; deviance explained = 19.3%) and peaked near $\sigma_0 \sim 27.44$ kg m^{-3} at Site W where denser water is observed ($R^2 = 0.067$; deviance explained = 7.0%), suggesting that nekton backscatter tracks an optimal UCDW fraction that differs among SCB basins. At Site H, DO was the significant predictor, with nekton backscatter increasing with higher DO ($R^2 = 0.04$; deviance explained = 4.3%). Overall deviance explained was low across all models, consistent with the multi-scale complexity evident in the spectral analysis.

Basin Flushing Events Coincide with Elevated Nekton Backscatter and *Z. cavirostris* Presence

Five flushing events were identified across Sites E and W between 2017 and 2023 (Table S4). Flushing events are defined here as rapid decreases in Θ ($\Delta\Theta \leq -0.1$ °C over 6 h) concurrent with increases in S_A and DO [19] and indicative of lateral intrusion of denser, more oxygenated water into the basin. Most events occurred between late August and October and were associated with increased UCDW fraction. No flushing events were observed at Site H, consistent with its shallower sill height limiting deep-water renewal and sustaining the severe hypoxia.

At Site E, the October 2017 flushing event increased the UCDW fraction from approximately 54% to 58% (Extended Data Fig. 5) and coincided with a subsequent increase in nekton backscatter, followed by increased *Z. cavirostris* acoustic presence (Fig. 5a). The event was preceded by declining sea surface temperature (SST) and a moderate upwelling signal of Coastal Upwelling Transport Index = 0.286 m^2 s^{-1} at 33°N (CUTI; [42]). A similar surface forcing sequence was observed prior to flushing events at Site W (Extended Data Fig. 4): SST decline at the end of the summer coinciding with an upwelling pulse immediately following a downwelling event.

On September 19th, 2017, an increase in water density also occurred but did not meet the criteria for classification as a flushing event. Conditions returned to their prior state within two weeks, reflecting a temporary vertical shift in water mass structure or incomplete mixing. This contrasts with the October 1st flushing event, which produced a greater than 2-month change in water mass properties at the microCAT sampling depth. In both cases, a less than 7-day downwelling period preceded basin ventilation.

Flushing events appear to occur following a sequence of physical processes: SST decreases, a period of downwelling occurs, and a subsequent upwelling event triggers the lateral exchange of denser, colder, and more oxygenated UCDW into the basin interior (Fig. 5b). Not all upwelling events, even those associated with equatorward meridional winds, result in isopycnals being uplifted sufficiently to initiate a flushing event. Instead, preconditioning of the water column prior to the upwelling event appears to be a critical factor, potentially linked to the preceding decrease in SST. Additionally, sill depth likely determines both the occurrence of flushing and the extent to which deep water masses are renewed, explaining the absence of flushing at Site H. Despite its proximity to Site E and otherwise similar water-mass composition (Extended Data Fig. 3), Site H has a shallower sill and exhibits persistent severe hypoxia, suggesting reduced connectivity with surrounding source waters.

Z. cavirostris Presence Tracks Shifts in Nekton Abundance and Target Strength

Acoustic detections of *Z. cavirostris* at Site E from 2017–2022 reveal a consistent seasonal pattern, with presence increasing in late fall and declining to near-zero in August–September across all years (Fig. 6a,c). When concurrent echosounder data are available, periods of elevated predator presence correspond with increased s_A, while declines align with reduced nekton backscatter (for example, July 2017). The October 2017 flushing event coincided with a shift toward a higher UCDW fraction, a subsequent increase in nekton backscatter, and an increase in *Z. cavirostris* acoustic detections (Fig. 5).

Weekly-binned median *TS* of putative nekton reveal seasonal structure in both the abundance and composition of the mid-trophic community (Fig. 6b). During late summer to early fall (approximately August–October, weeks 31–44 of the year), nekton abundance decreased across both *TS* modes, coinciding with the annual minimum in *Z. cavirostris* presence (Fig. 6c). In contrast, during winter and early spring, a higher-*TS* mode (−49.75 dB re 1 m^2) and a lower-*TS* mode (−52.4 dB re 1 m^2) co-occurred at elevated abundance, coinciding with peak predator presence. This seasonal co-occurrence of two *TS* modes may reflect overlapping prey communities of different size classes, taxa, or life-history stages within the same assemblage. The nekton minimum in late summer therefore reflects not only reduced overall abundance but a near-complete absence of both components of the mid-trophic community backscatter.

Interannual variability is also evident. In October 2018, *Z. cavirostris* presence remained relatively stable (∼100 min day^{-1}) rather than exhibiting the typical late-fall peak (>150 min day^{-1}), potentially reflecting interannual differences in UCDW influx and associated nekton response.

Together, these patterns demonstrate that *Z. cavirostris* presence at Site E is associated with increased nekton abundance across *TS* values, and that episodic physical forcing events, overlapping with tidal and

seasonal variability, produce a dynamic mid-trophic nekton community within which this highly mobile predator forages.

Discussion

The three study sites span a gradient of physical connectivity and oxygenation reflecting their contrasting basin bathymetries. Site W, the deepest and most open-ocean-exposed site, maintained the highest DO, consistent with frequent exchange of oxygenated deep water across its relatively deep sills. Site E, within Tanner Basin, experienced intermediate and variable DO conditions, with episodic flushing events periodically renewing deep water and increasing the proportion of UCDW. Site H, enclosed within San Nicolas Basin by comparatively shallow sills, was persistently and severely hypoxic throughout the 2022–2023 deployment period, with no flushing events observed. Despite geographic proximity (∼125 km separation), the three sites maintained distinct hydrographic conditions and biological communities, suggesting that sill-controlled exchange and basin connectivity contribute to ecological differentiation among SCB basins.

By integrating multi-year, fine-scale (h–seasons, <100 km) *in situ* observations, this study characterizes hydrographic variability and associated shifts in bathypelagic biological communities within and among SCB basins, and examines how these patterns correspond with the presence of foraging *Z. cavirostris*. Persistent differences in water mass properties, DO, s_A, organism *TS* distributions, and cephalopod family eDNA indicate that bathypelagic environments in the SCB are not equivalent. Although eDNA samples were collected only during spring and fall cruises and aggregated by site and depth, preventing assessment of seasonal and vertical variability in cephalopod composition, site-level differences were evident: Sites E and W were dominated by Gonatidae, whereas Site H supported a proportionally greater Histioteuthidae community, likely reflecting greater tolerance of persistently hypoxic conditions.

Flushing events were associated with some of the strongest biological responses observed in this dataset. At Site E, the October 2017 flushing event increased the UCDW fraction from approximately 54% to 58%, introducing more oxygenated water into the basin and coinciding with elevated nekton backscatter followed by increased *Z. cavirostris* acoustic detections. This response is consistent with oxygen limitation near the severe hypoxia threshold (DO $\leq$ 0.5 mL L^{-1}): Site H maintained similar water-mass fractions characterized by Θ andS_A but experienced no flushing and persistently low oxygen, while Site W experienced more frequent flushing and remained consistently above this threshold without comparable increases in nekton backscatter. Together, these contrasts suggest that oxygen renewal becomes biologically important primarily under near-hypoxic baseline conditions.

We hypothesize that basin ventilation depends on a specific sequence of oceanographic processes rather than upwelling intensity alone. Not all upwelling events produced flushing, suggesting that additional preconditions must be met for upwelled isopycnals to reach sill depth and allow denser, colder, more oxygenated UCDW to spill into adjacent basins. Coastal-driven upwelling appears to be a plausible and potentially consistent ventilation mechanism in some SCB basins, but the precise combination of preconditions remains unclear. Other mesoscale features, such as cyclonic eddies, could similarly drive flushing if they elevate isopycnals to sill height. Basin bathymetry likely modulates both the occurrence and magnitude of flushing, explaining the absence of ventilation at Site H despite its proximity to Site E and similar water-mass structure. The limited number of observed events constrains interpretation, and additional observations across basins and years are needed to better constrain the physical mechanisms and their ecological impacts.

Internal waves provided an additional modulating mechanism, generating tidal-frequency oscillations in backscatter at Sites W and H that likely reflect advection through the echosounder sampling volume rather than changes in total biomass. Considered together, these results indicate that bathypelagic habitat quality in the SCB is structured across nested timescales, with basin bathymetry setting baseline hydrographic conditions and tidal, seasonal, and episodic processes modulating biological community composition and abundance through time.

Several observational constraints were considered during interpretation of results. Discontinuous records from deployment delays and instrument failures limited temporal coverage, and the single-frequency 70 kHz echosounders provided limited taxonomic discrimination. Differences in beamwidth and mooring location preclude direct comparison of s_A values between sites. Passive acoustic detect *Z. cavirostris* over horizontal ranges of approximately 2–3 km, whereas echosounders insonify 7–18° cone-shaped volumes, consequently

Z. cavirostris may be detected while foraging outside the echosounder sampling volume; however, given that midwater biological patches are estimated at 2–4 km [43], temporal averaging over days to weeks likely captures variability even without complete spatial alignment. This study also did not evaluate temporal lags between surface forcing and deep-basin responses, which remain difficult to resolve even with long-term datasets [26, 44]. Future work would benefit from broadband, full-depth echosounder observations to improve taxonomic and size resolution and better resolve how hydrographic transitions modulate bathypelagic biological communities and predator foraging activity.

These findings indicate that basin bathymetry, particularly sill depth, governs the frequency and magnitude of deep-water exchange and thereby contributes to structuring bathypelagic biological communities within the SCB. Neighboring basins that differ in sill height, recurrence of ventilation events, and oxygenation can therefore constitute distinct bathypelagic habitats. The deep ocean is not a uniformly structured environment, but rather a mosaic of habitats whose biologically relevant hydrographic conditions emerge from variations in physical exchange and retention.

Methods

In situ hydrographic observations

The MicroCATs recorded pressure, Θ, S_A, and DO at 15-min intervals throughout each deployment, typically within ∼50 m depth of the echosounder sampling volume. 2017–2018 deployments at Site E sampled at 6-min intervals but were aggregated to a common 1-h analysis interval. All instruments were factory-calibrated prior to deployment and configured using SeaTermV2 (v2.8.0.119).

MicroCAT data were processed using SBE Data Processing (v7.26.7) and subsequently analyzed in `R` (v4.2.3) using the `read.cnv.file` function [45]. Raw temperature (IPTS-90) and salinity (practical salinity units) were converted to Θ and S_A using the `oce` package [46]. Deployment and recovery periods and outliers were removed, and inter-deployment offsets were corrected using overlapping conditions from the preceding deployment. σ_0 (kg m^{-3}) was calculated from Θ and S_A as $\sigma_0 = \rho(S_A, \Theta, 0) - 1000$, where ρ is seawater density in kg m^{-3} referenced to surface pressure (0). For time series visualization, σ_0 was daily-averaged and binned into 0.005 kg m^{-3} intervals.

MicroCAT records located more than 150 m from the WBAT sampling depth range but still <1000 m depth were excluded from echosounder–hydrographic comparisons (e.g., Site W, March 2022), as they were not considered representative of conditions experienced by acoustically sampled prey layers, but were retained for independent analysis of hydrographic conditions including the identification of flushing events. Mean instrument depth was calculated from pressure records, and deviations from this mean were used to correct for vertical mooring motion in echosounder analysis. Further details on sensor accuracy, calibration, and offset corrections are provided in the Supplementary Methods (Table S5).

Water mass structure and source attribution

To characterize hydrographic variability in terms of source water composition, we applied an Optimum Multiparameter (OMP) framework to estimate fractional contributions of NPIW, AAIW, and UCDW from daily-averaged Θ and S_A observations. Although limited to two tracers, this approach provides a first-order characterization of water mass variability across the time series. The framework followed established OMP formulations [47, 18] previously applied in the SCB [26]. End-member Θ and S_A properties were derived from the World Ocean Atlas 2023 (WOA23) annual climatology [48, 49] at 33°N, 120°W to reflect regional, North Pacific-modified conditions, with isopycnal surfaces and depth ranges defined using canonical definitions [24] as implemented in a prior study [25] (Table S6). Although NPIW, AAIW, and UCDW occupy overlapping depth ranges in the North Pacific, they are distinguished by their characteristic isopycnal surfaces and salinity structure: NPIW forms the shallowest salinity minimum at $\sigma_0 \approx 26.8$, AAIW has a deeper salinity minimum at $\sigma_0 \approx 27.1$, and UCDW is characterized by a relatively high salinity on the $\sigma_0 \approx 27.6$ isopycnal [24]. PDW occupies a similar depth and density range to UCDW but was excluded as the deep end member because concurrent mooring DO observations showed elevated oxygen during cold, dense, high-salinity intrusion events, consistent with UCDW rather than the oxygen-minimum signature of PDW [24]. Fractional contributions were estimated using non-negative least squares with a mass conservation constraint. Observations closely

followed the climatological WOA23 Θ–S_A relationship at the selected grid location (Extended Data Fig. 5); residuals were small (S_A RMSE = 0.027 g kg^{-1}, bias = +0.023 g kg^{-1}; Θ RMSE = 0.12 °C, bias = −0.10 °C), likely reflecting local modification of source waters within the semi-enclosed SCB basins rather than systematic end-member misspecification. NPIW fractions were negligible across all three sites and excluded from further analysis.

Hydrographic flushing event identification and physical forcing

Flushing events were defined as rapid decreases in Θ ($\Delta\Theta \leq -0.1$ °C over 6 h) concurrent with increases in S_A and DO. This signal is consistent with the introduction of denser, more oxygenated water into the basin interior [19]. All ventilation events meeting these criteria are reported in Table S4; only those with concurrent NOAA buoy [50] and CUTI [42] coverage were retained for atmospheric forcing comparisons.

Atmospheric and surface ocean conditions were characterized using data from NOAA National Data Buoy Center stations 46219 (San Nicolas Island, CA) for Site E and 46069 (South Santa Rosa Island, CA) for Site W [50]. Wind vectors were converted to meridional wind velocity. Upwelling intensity was characterized using the CUTI at 33°N [42]. Environmental data were extracted over an 8-week pre- and post-event window to characterize the forcing conditions.

Environmental DNA sampling

eDNA samples were collected from Sites E, H, and W in May and October 2022, and from Site W again in April 2023, aboard the R/V *Gordon Sproul*. At each site, 2 L of seawater was sampled using Niskin bottles mounted on a CTD rosette. Within 1 h of recovery, all samples were filtered onto Sterivex filters and stored at −80°C until processing.

DNA extraction used a phenol/chloroform/isoamyl alcohol protocol. Extracted DNA was diluted (1:10) prior to amplification of cephalopod nuclear 18S rRNA gene fragments using the Ceph18S primer set [51]. Library preparation and sequencing were conducted at the Georgia Genomics and Bioinformatics Core (GGBC; University of Georgia, Athens, GA; RRID:SCR010994) on an Illumina NextSeq 2000 platform using a P1 XLEAP-SBS 600-cycle reagent kit, generating 300 bp paired-end reads. Sequence reads were summarized per site across deep CTD stations (500 m to near-bottom) and aggregated to family-level taxonomic resolution.

Nekton backscatter quantification

Acoustic backscatter was processed to isolate putative nekton, a proxy for prey biomass [52, 8, 53, 43]. Each WBAT transmitted 70-kHz continuous-wave (CW) pulses with a duty cycle configured to extend deployment duration (3–6 months); deployment-specific configurations are provided in Table S7. At Sites H, E, and W (Fig. 1c), the transducer was deployed approximately 50 m above the seafloor and projected upward. At Site W (March 2022), the transducer was approximately 500 m above the seafloor and projected downward. Depending on the transducer beamwidth (ES70-18CD or ES70-7CD; Kongsberg, Norway), backscatter was analyzed within 125 or 300 m of the transducer. The precise depths of the transducers, and therefore the backscatter samples, were improved using pressure time-series from the MicroCATs.

Backscatter data were processed in Echoview (v14.0.227, Echoview Software Pty Ltd, Hobart, Tasmania) using functions from *EchoviewR* [54] and the Echoview COM automation interface to enable reproducible processing pipelines in `R` (v4.2.3). Processing included removal of near-field data (0–10 m from the transducer) and correction for transducer depth and mooring geometry. Sound speed was calculated from deployment-mean Θ and S_A using the Chen–Millero equation [55]. Echosounder systems were calibrated using a 38.1 mm tungsten carbide sphere [56, 57]; calibration procedures and results are reported in Fig. S1 and Table S7.

After removal of transient noise and impulse artifacts [58, 59], a *TS* threshold of −55 to −40 dB re 1 m^2 was applied to isolate putative prey signals, including weakly scattering organisms such as cephalopods [60, 61, 62, 63, 8]. Because this threshold is applied to apparent *TS* derived from volume backscatter rather than verified single targets, it implicitly constrains both the *TS* values and the density of scatterers contributing to the integrated signal. However, backscatter in these bathypelagic environments was dominated by low-density, spatially dispersed targets; the *TS* threshold therefore primarily restricts the range of *TS* values

rather than excluding dense aggregations, which were absent from these data. s_A; m^2 nmi^{-2} were exported in 1-m depth and 1-h time bins. s_A >3 SD from the site mean were removed prior to analysis.

Individual nekton were detected and tracked independently of the s_A integration pipeline using Echoview's 4D single-target detection and tracking algorithms, configured for low-density, non-overlapping targets. Median *TS* was computed per track, yielding one value per putative individual organism. The transducer ranges used for analysis (125 or 300 m depending on transducer type) were applied consistently across both s_A and *TS* analyses (Fig. S2).

The two transducer models differ in beamwidth (7° and 18°), and both sample a volume smaller than the nekton patches. Measured backscatter may therefore be influenced by instrument placement relative to local bathymetric features and current patterns, and may not reflect basin-wide prey abundance. For example, a transducer positioned away from a slope or sill where currents preferentially aggregate nekton may underestimate local prey availability to *Z. cavirostris*. Three-dimensional tracks of *Z. cavirostris* indicate spatial preferences within basins, suggesting nekton patches may persist in predictable patterns shaped by basin bathymetry [64]. Analyses therefore emphasized intra-site s_A variability rather than inter-site magnitude. Relationships between hydrographic conditions and both s_A and organism *TS* are compared across sites.

Z. cavirostris acoustic presence

Daily *Z. cavirostris* acoustic detections were quantified from High-Frequency Acoustic Recording Package (HARP) data recorded at a 200 kHz sampling rate [39]. All *Z. cavirostris* click detections were processed using the open-source *Triton* software package [65]. Labels were manually reviewed and confirmed in *DetEdit* [66].

Site E deployments from 2017–2018 were processed using custom routines in MATLAB 2013b (MathWorks Inc., Natick, Massachusetts), with *Z. cavirostris* clicks separated from delphinid clicks following established methods [67, 68]. Subsequent Site E deployments (2021–2022) were processed using a Butterworth bandpass filter and a two-phase unsupervised clustering algorithm [69, 70], followed by a neural network classifier [64] trained to recognize echolocation clicks from *Z. cavirostris* and co-occurring delphinid species [71, 72, 73], as well as anthropogenic signals. Both methods were processed with a peak-to-peak received level threshold of 121 dB re 1 µPa. A subsample of Site E data processed by both methods revealed minimal differences: the neural network identified an average of 7 min 45 s more *Z. cavirostris* acoustic presence per day ($n = 68$), likely reflecting its superior detection of lower-amplitude signals.

Echolocation click detections were binned into 1-min presence–absence intervals and summed daily.

Statistical analysis

Generalized Additive Models

GAMs were used to investigate relationships between nekton backscatter and environmental conditions at Sites E, H, and W, fitted using the `mgcv` package [74] in `R` (v4.2.3). Temporal autocorrelation in s_A was assessed via autocorrelation functions of Poisson GLM residuals, and data were subsequently aggregated into site-specific temporal bins based on the first non-significant autocorrelation lag (Site H: 19 h, Site E: 83 h, Site W: 78 h). Within each bin, mean values of Θ (°C), S_A (g kg^{-1}), DO (mL L^{-1}), σ_0 (kg m^{-3}), and s_A were calculated. Due to strong collinearity among hydrographic variables, a single primary predictor was selected per site. Density (σ_0) was used at Sites E and W, as not all microCATs were equipped with DO sensors, allowing more data points to be included in the analysis. DO was used at Site H given persistent hypoxic conditions and the limited explanatory power of σ_0 in preliminary models. GAMs were fitted with Tweedie error distributions and thin-plate regression splines with shrinkage (`bs = "ts"`), with smoothing parameters estimated by restricted maximum likelihood (REML). Basis dimensions were selected by minimum AIC from candidate values ($k \in \{3, 4, 5, 6\}$), yielding $k = 6$ at Sites E and W and $k = 4$ at Site H. Basis dimension adequacy was verified using `gam.check()`.

Spectral Analysis

Spectral density analyses identified dominant temporal periodicities in σ_0 and s_A across Sites E, H, and W. For each site, the longest continuous period with simultaneous environmental and acoustic observations was identified. Short gaps ($\leq$3 h) were linearly interpolated to preserve temporal continuity; extended data gaps were not interpolated. Time series were standardized by removing the mean. Spectral power density was estimated using a smoothed periodogram (`R` function `spectrum` from the `stats` package) with a 10% cosine taper and Welch-type smoothing with modified Daniell spans (5, 5). Confidence intervals (95%) intervals were computed from the chi-squared distribution using the effective degrees of freedom returned by `spectrum`. Analyses were restricted to periodicities between 6 h and 30 d. Durations of continuous time series used for spectral analysis are provided in Table S8.

Target Strength Distribution Comparisons

To evaluate whether distributions of median *TS* of putative nekton differed significantly among sites, a Kruskal-Wallis test was first applied to data across all three sites, followed by pairwise Wilcoxon rank-sum tests with Benjamini-Hochberg correction for multiple comparisons. Median and interquartile range (IQR) were used as measures of central tendency and spread, as both are order statistics that transform consistently across the logarithmic *TS* scale and are aligned with the rank-based tests applied. All analyses were performed in `R` (v4.2.3). Test statistics and adjusted p-values are reported in Fig. 3c.

Manuscript Preparation

In preparing this manuscript, we used Claude (Anthropic; Sonnet 4.6) to assist with code debugging and manuscript editing. All AI-assisted material was edited and validated, and we take full responsibility for the final content.

Data availability

The data analyzed for this study are available in the DRYAD repository, DOI `10.5061/dryad.2547d7x6m`.

Code availability

Code is available on GitHub at `https://github.com/shannon-dolan/MultiMooringMonitoring`.

Acknowledgments

We thank the crew of the R/V Sally Ride, R/V Robert Gordon Sproul, and R/V Bob and Betty Beyster for assistance with mooring deployments. We thank members of the Marine Bioacoustics Research Collaborative including B. Thayre, K. Lenssen, J. Hurwitz, J. Trickey, and S. Bloom for assistance with instrumentation and xwav processing. This material is based upon work supported by the Air Force Office of Scientific Research under award number FA9550-23-F-0014. We thank Mike Weise and the Office of Naval Research (awards N000142014000 and N000142312435), as well as Chip Johnson and Christiana Salles through the California Cooperative Ecosystems Studies Unit under agreement with the U.S. Navy, U.S. Pacific Fleet (award N000142112611), for their support of this work.

Author contributions statement

S.M.D. participated in fieldwork, processed all echosounder, MicroCAT, NOAA buoy data, and a portion of the hydrophone data, performed all statistical tests, and generated all figures. A.S.B. contributed project conceptualization and supervision. C.M.B. provided code for OMP analysis and participated in fieldwork. L.M.B. processed hydrophone data and participated in fieldwork. A.S., J.D.W., and S.B.P. acquired funding for the project and participated in fieldwork. J.D.W. and D.A.D. supervised echosounder analyses. S.T.G.

provided physical oceanography expertise. J.D. processed all eDNA data. S.B.P. led project conceptualization and supervision. S.M.D. wrote the first draft of the manuscript, with editorial contributions from all other authors.

Additional information

Competing interests: The authors declare no competing interests.

References

[1] Tyack, P. L., Johnson, M., Soto, N. A., Sturlese, A. & Madsen, P. T. Extreme diving of beaked whales. *J Exp Biol* **209**, 4238–4253 (2006).

[2] Johnson, M., Madsen, P. T., Zimmer, W. M., de Soto, N. A. & Tyack, P. L. Beaked whales echolocate on prey. *Proc Biol Sci* **271 Suppl 6**, 383–6 (2004).

[3] West, K. L., Walker, W. A., Baird, R. W., Mead, J. G. & Collins, P. W. Diet of Cuvier's beaked whales Ziphius cavirostris from the North Pacific and a comparison with their diet world-wide. *Marine Ecology Progress Series* **574**, 227–242 (2017).

[4] Schorr, G. S., Falcone, E. A., Moretti, D. J. & Andrews, R. D. First long-term behavioral records from Cuvier's beaked whales (Ziphius cavirostris) reveal record-breaking dives. *PLoS One* **9**, e92633 (2014).

[5] Falcone, E. A. *et al.* Sighting characteristics and photo-identification of Cuvier's beaked whales (Ziphius cavirostris) near San Clemente Island, California: a key area for beaked whales and the military? *Marine Biology* **156**, 2631–2640 (2009).

[6] Hazen, E. L., Nowacek, D. P., St. Laurent, L., Halpin, P. N. & Moretti, D. J. The relationship among oceanography, prey fields, and beaked whale foraging habitat in the Tongue of the Ocean. *PLoS One* **6**, e19269 (2011).

[7] Benoit-Bird, K. J. Resource patchiness as a resolution to the food paradox in the sea. *The American Naturalist* **203**, 1–13 (2024).

[8] Southall, B. L., Benoit-Bird, K. J., Moline, M. A., Moretti, D. & Januchowski-Hartley, S. Quantifying deep-sea predator–prey dynamics: Implications of biological heterogeneity for beaked whale conservation. *Journal of Applied Ecology* **56**, 1040–1049 (2019).

[9] Capet, X., Mcwilliams, J. C., Molemaker, M. J. & Shchepetkin, A. F. Mesoscale to submesoscale transition in the California Current System. Part I: Flow structure, eddy flux, and observational tests. *Journal of Physical Oceanography* **38**, 29–43 (2008).

[10] Bray, N. A., Keyes, A. & Morawitz, W. M. L. The California current system in the Southern California bight and the Santa Barbara Channel. *Journal of Geophysical Research: Oceans* **104**, 7695–7714 (1999).

[11] Hickey, B. M., Dobbins, E. L. & Allen, S. E. Local and remote forcing of currents and temperature in the central Southern California Bight. *Journal of Geophysical Research: Oceans* **108** (2003).

[12] Lynn, R. J. & Simpson, J. J. The California Current System: The seasonal variability of its physical characteristics. *Journal of Geophysical Research: Oceans* **92**, 12947–12966 (1987).

[13] Chavez, F. P. & Messié, M. A comparison of eastern boundary upwelling ecosystems. *Progress in Oceanography* **83**, 80–96 (2009).

[14] Dong, C. *et al.* Three-dimensional oceanic eddy analysis in the Southern California Bight from a numerical product. *Journal of Geophysical Research: Oceans* **117** (2012).

[15] Hall, R. A. & Carter, G. S. Internal Tides in Monterey Submarine Canyon. *Journal of Physical Oceanography* **41**, 186–204 (2011).

[16] Kunze, E., Rosenfeld, L. K., Carter, G. S. & Gregg, M. C. Internal waves in Monterey submarine canyon. *Journal of physical oceanography* **32**, 1890–1913 (2002).

[17] Allen, S. E. & Hickey, B. M. Dynamics of advection-driven upwelling over a shelf break submarine canyon. *Journal of Geophysical Research: Oceans* **115** (2010).

[18] Bograd, S. J., Schroeder, I. D. & Jacox, M. G. A water mass history of the Southern California current system. *Geophysical Research Letters* **46**, 6690–6698 (2019).

[19] McWilliams, J. C., Damien, P. & Kessouri, F. Circulation and dispersal in California's Borderland Basins. *Progress in Oceanography* **229**, 103349 (2024).

[20] Berelson, W. M. The flushing of two deep-sea basins, southern California borderland. *Limnology and oceanography* **36**, 1150–1166 (1991).

[21] Robinson, D., Bianchi, D., Liu, N., Valentine, D. L. & Treude, T. Spatial Distribution and Temporal Variability of Dissolved O2 in the Santa Barbara Channel and Basin, California. *Journal of Geophysical Research: Oceans* **131**, e2025JC022779 (2026).

[22] Messié, M. *et al.* Coastal upwelling drives ecosystem temporal variability from the surface to the abyssal seafloor. *Proceedings of the National Academy of Sciences* **120**, e2214567120 (2023).

[23] Pearman, T. R. R. *et al.* Spatial and temporal environmental heterogeneity induced by internal tides influences faunal patterns on vertical walls within a submarine canyon. *Frontiers in Marine Science* **10**, 1091855 (2023).

[24] Talley, L. D. *Descriptive physical oceanography: an introduction* (Academic press, 2011).

[25] Kolody, B. C. *et al.* Overturning circulation structures the microbial functional seascape of the South Pacific. *Science* **389**, 176–182 (2025).

[26] Schoenbeck, C. M. *et al.* Ziphius cavirostris presence relative to the vertical and temporal variability of oceanographic conditions in the Southern California Bight. *Ecology and Evolution* **14**, e11708 (2024).

[27] Hoving, H.-J. T. & Robison, B. H. The pace of life in deep-dwelling squids. *Deep Sea Research Part I: Oceanographic Research Papers* **126**, 40–49 (2017).

[28] McSweeney, D. J., Baird, R. W. & Mahaffy, S. D. Site fidelity, associations, and movements of Cuvier's (Ziphius cavirostris) and Blainville's (Mesoplodon densirostris) beaked whales off the island of Hawai 'i. *Marine Mammal Science* **23**, 666–687 (2007).

[29] Baird, R. W. Behavior and Ecology of Not-So-Social Odontocetes: Cuvier's and Blainville's Beaked Whales. In *Ethology and Behavioral Ecology of Odontocetes*, 305–329 (2019).

[30] MacLeod, C. D., Santos, M. B. & Pierce, G. J. Review of data on diets of beaked whales: evidence of niche separation and geographic segregation. *Journal of the Marine Biological Association of the United Kingdom* **83**, 651–665 (2003).

[31] Vidal, E. A. G. & Shea, E. K. Cephalopod ontogeny and life cycle patterns. *Frontiers in Marine Science* **10**, 1162735 (2023).

[32] Hoving, H.-J. T. *et al.* The study of deep-sea cephalopods. *Advances in marine biology* **67**, 235–359 (2014).

[33] Seibel, B. A., Robison, B. H. & Haddock, S. H. D. Post-spawning egg care by a squid. *Nature* **438**, 929 (2005).

[34] Seibel, B. A., Thuesen, E. V., Childress, J. J. & Gorodezky, L. A. Decline in pelagic cephalopod metabolism with habitat depth reflects differences in locomotory efficiency. *The biological bulletin* **192**, 262–278 (1997).

[35] Ikeda, T. Routine metabolic rates of pelagic marine fishes and cephalopods as a function of body mass, habitat temperature and habitat depth. *Journal of Experimental Marine Biology and Ecology* **480**, 74–86 (2016).

[36] Rodgveller, C. J., Clausen, D. M., Nagler, J. J. & Hutchinson, C. Reproductive characteristics and mortality of female giant grenadiers in the northern Pacific Ocean. *Marine and coastal fisheries* **2**, 73–82 (2010).

[37] Cade, D. E. *et al.* Predator-scale spatial analysis of intra-patch prey distribution reveals the energetic drivers of rorqual whale super-group formation. *Functional Ecology* **35**, 894–908 (2021).

[38] Xing, Q., Yu, H., Wang, H., Ito, S.-i. & Yu, W. Mesoscale eddies exert inverse latitudinal effects on global industrial squid fisheries. *Science of The Total Environment* **950**, 175211 (2024).

[39] Wiggins, S. M. & Hildebrand, J. A. High-frequency Acoustic Recording Package (HARP) for broadband, long-term marine mammal monitoring. In *2007 symposium on underwater technology and workshop on scientific use of submarine cables and related technologies*, 551–557 (IEEE, 2007).

[40] Levin, L. A. Oxygen minimum zone influence on the community structure of deep-sea benthos. In *Proceedings of the sixth international symposium on fish physiology, toxicology, and water quality*, 121–133 (2002).

[41] Maren, D. & Gerritsen, H. Residual flow and tidal asymmetry in the Singapore Strait, with implications for resuspension and residual transport of sediment. *Journal of Geophysical Research* **117** (2012).

[42] Jacox, M. G., Edwards, C. A., Hazen, E. L. & Bograd, S. J. Coastal upwelling revisited: Ekman, Bakun, and improved upwelling indices for the U.S. west coast. *Journal of Geophysical Research: Oceans* **123**, 7332–7350 (2018).

[43] Grassian, B., Roman, C., Warren, J. D. & Casagrande, D. High-resolution measurements of the epipelagic and mesopelagic ocean by a profiling vehicle equipped with environmental sensors and a broadband echosounder. *Limnology and Oceanography: Methods* **21**, 106–125 (2023).

[44] Benoit-Bird, K. J., Southall, B. L. & Moline, M. A. Predator-guided sampling reveals biotic structure in the bathypelagic. *Proceedings of the Royal Society B: Biological Sciences* **283**, 20152457 (2016).

[45] Lipka, M. & Kaiser, D. readCNV (2021).

[46] Kelley, D. & Richards, C. oce: Analysis of Oceanographic Data (2026).

[47] Tomczak, M. & Large, D. G. B. Optimum multiparameter analysis of mixing in the thermocline of the eastern Indian Ocean. *Journal of Geophysical Research: Oceans* **94**, 16141–16149 (1989).

[48] Locarnini, R. *et al.* World Ocean Atlas 2023, Volume 1: Temperature. Tech. Rep. 89, NOAA (2023). URL `https://doi.org/10.25923/54bh-1613`.

[49] Reagan, J. *et al.* World Ocean Atlas 2023, Volume 2: Salinity. Tech. Rep. 90, NOAA (2023). URL `https://doi.org/10.25923/70qt-9574`.

[50] NOAA National Data Buoy Center. Meteorological and oceanographic data collected from the National Data Buoy Center Coastal-Marine Automated Network (C-MAN) and moored (weather) buoys.

[51] de Jonge, D. S. W. *et al.* A novel metabarcoding primer pair for environmental DNA analysis of Cephalopoda (Mollusca) targeting the nuclear 18S rRNA region. *Royal Society Open Science* **8**, 201388 (2021).

[52] Proud, R., Handegard, N. O., Kloser, R. J., Cox, M. J. & Brierley, A. S. From siphonophores to deep scattering layers: uncertainty ranges for the estimation of global mesopelagic fish biomass. *ICES Journal of Marine Science* **76**, 718–733 (2018).

[53] Urmy, S. S., Horne, J. K. & Barbee, D. H. Measuring the vertical distributional variability of pelagic fauna in Monterey Bay. *ICES Journal of Marine Science* **69**, 184–196 (2012).

[54] Harrison, L.-M. K., Cox, M. J., Skaret, G. & Harcourt, R. The R package EchoviewR for automated processing of active acoustic data using Echoview. *Frontiers in Marine Science* **2** (2015).

[55] Chen, C. & Millero, F. J. Speed of sound in seawater at high pressures. *The Journal of the Acoustical Society of America* **62**, 1129–1135 (1977).

[56] Simmonds, J. & MacLennan, D. N. *Fisheries acoustics: theory and practice* (John Wiley & Sons, 2008).

[57] Demer, D. A. *et al.* Calibration of acoustic instruments (2015).

[58] Ryan, T. E., Downie, R. A., Kloser, R. J. & Keith, G. Reducing bias due to noise and attenuation in open-ocean echo integration data. *ICES Journal of Marine Science* **72**, 2482–2493 (2015).

[59] De Robertis, A. & Higginbottom, I. A post-processing technique to estimate the signal-to-noise ratio and remove echosounder background noise. *ICES Journal of Marine Science* **64**, 1282–1291 (2007).

[60] Benoit-Bird, K. J., Gilly, W. F., Au, W. W. L. & Mate, B. Controlled and in situ target strengths of the jumbo squid Dosidicus gigas and identification of potential acoustic scattering sources. *The Journal of the Acoustical Society of America* **123**, 1318–1328 (2008).

[61] Kang, D., Mukai, T., Iida, K., Hwang, D. & Myoung, J.-G. The influence of tilt angle on the acoustic target strength of the Japanese common squid (Todarodes pacificus). *ICES Journal of Marine Science* **62**, 779–789 (2005).

[62] Lee, W.-J., Lavery, A. C. & Stanton, T. K. Orientation dependence of broadband acoustic backscattering from live squid. *The Journal of the Acoustical Society of America* **131**, 4461–4475 (2012).

[63] Villalobos, H., Manini-Ramos, F., Salinas-Zavala, C. & Brehmer, P. Jumbo squid (Dosidicus gigas) in situ target strength measurements in northwest Mexico. In *2013 IEEE/OES Acoustics in Underwater Geosciences Symposium*, 1–3 (2013).

[64] Baggett, L. M. *et al.* Long-term monitoring of Ziphius cavirostris behavior using 3D tracking from fixed hydrophone arrays off Southern California. *Scientific Reports* **15**, 40859 (2025).

[65] Marine BioAcoustics Research Collaborative. Triton Software Package (2019).

[66] Solsona-Berga, A., Frasier, K. E., Baumann-Pickering, S., Wiggins, S. M. & Hildebrand, J. A. DetEdit: A graphical user interface for annotating and editing events detected in long-term acoustic monitoring data. *PLOS Computational Biology* **16**, e1007598 (2020).

[67] Trickey, J. S. *et al.* Ultrasonic antifouling devices negatively impact Cuvier's beaked whales near Guadalupe Island, Mexico. *Commun Biol* **5**, 1005 (2022).

[68] Baumann-Pickering, S. *et al.* Species-specific beaked whale echolocation signals. *J Acoust Soc Am* **134**, 2293–2301 (2013). URL `https://www.ncbi.nlm.nih.gov/pubmed/23967959`.

[69] Frasier, K. E. *et al.* Automated classification of dolphin echolocation click types from the Gulf of Mexico. *PLOS Computational Biology* **13**, e1005823 (2017).

[70] Frasier, K. E. A machine learning pipeline for classification of cetacean echolocation clicks in large underwater acoustic datasets. *PLOS Computational Biology* **17**, e1009613 (2021).

[71] Soldevilla, M. S. *et al.* Classification of Risso's and Pacific white-sided dolphins using spectral properties of echolocation clicks. *The Journal of the Acoustical Society of America* **124**, 609–624 (2008).

[72] Zimmer, W. M., Harwood, J., Tyack, P. L., Johnson, M. P. & Madsen, P. T. Passive acoustic detection of deep-diving beaked whales. *J Acoust Soc Am* **124**, 2823–2832 (2008).

[73] Zimmer, W. M., Johnson, M. P., Madsen, P. T. & Tyack, P. L. Echolocation clicks of free-ranging Cuvier's beaked whales (Ziphius cavirostris). *J Acoust Soc Am* **117**, 3919–3927 (2005).

[74] Wood, S. N. Fast stable restricted maximum likelihood and marginal likelihood estimation of semiparametric generalized linear models. *Journal of the Royal Statistical Society (B)* **73**, 3–36 (2011).

[75] GEBCO Bathymetric Compilation Group 2023. The GEBCO_2023 Grid - a continuous terrain model of the global oceans and land.

[76] Mauzole, Y., Torres, H. & Fu, L.-L. Patterns and Dynamics of SST Fronts in the California Current System. *Journal of Geophysical Research: Oceans* **125** (2020).

[77] Reid, J. L. Studies of the California Current system. *Cal. Coop. Oc. Fish. Invest.* **1**, 28–56 (1958).

[78] Thyng, K. M., Greene, C. A., Hetland, R. D., Zimmerle, H. M. & DiMarco, S. F. True colors of oceanography: Guidelines for effective and accurate colormap selection. *Oceanography* **29**, 9–13 (2016).

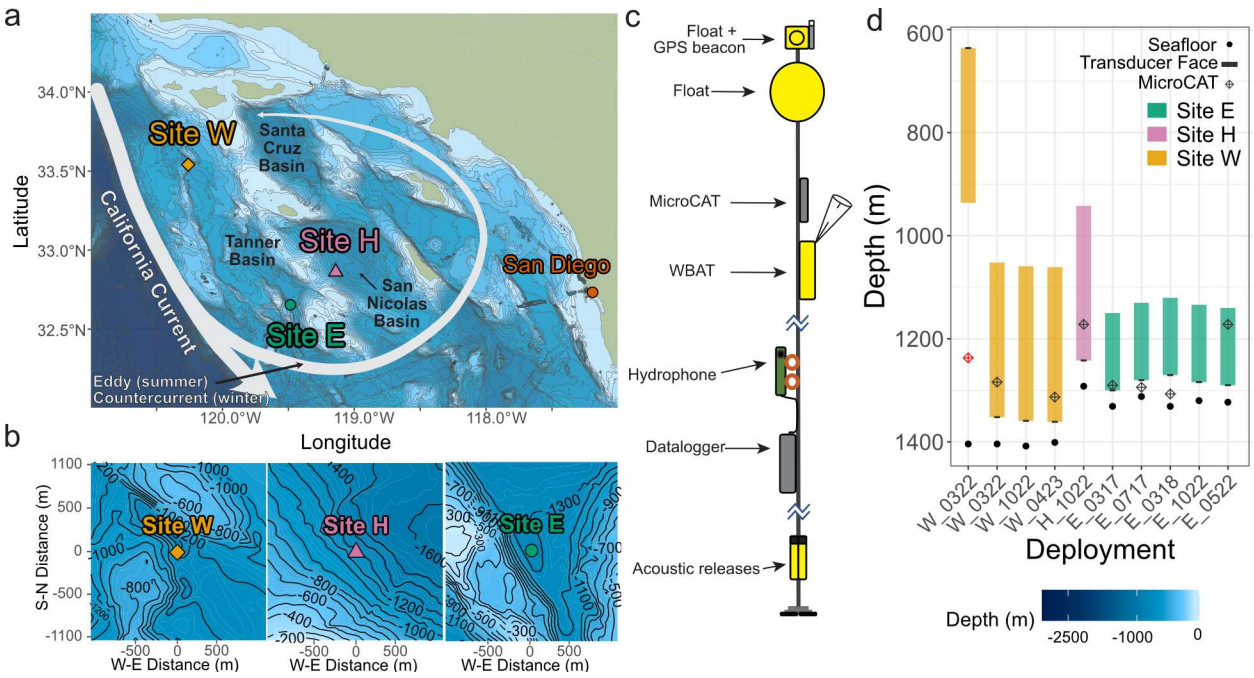

Fig. 1 — Study sites and mooring configuration in the Southern California Bight. **(a)** Map showing mooring locations at Sites W (orange diamond), H (pink triangle), and E (green circle), with 100 m bathymetric contours derived from GEBCO data [75]. Major oceanographic features are indicated, including the California Current, the Southern California Eddy (summer), and the Southern California Countercurrent (winter), adapted from refs. [76, 77]. **(b)** Local bathymetry within a 0.2° region around each site, with N-S and W-E distances in meters relative to the mooring position. **(c)** Schematic of the multi-instrument mooring configuration with the MicroCAT oceanographic sensors, WBAT echosounder, and HARP hydrophone. **(d)** Deployment-specific WBAT depths at Sites W (orange), H (pink), and E (green). Bars indicate the WBAT sampling range; filled circles show seafloor depth; open diamonds show MicroCAT deployment depths; horizontal dashes indicate the transducer face depth. MicroCATs located more than 150 m from the WBAT sampling range are shown with open red diamonds and were excluded from selected analyses. Deployments are labeled by site and month-year (MMYY).

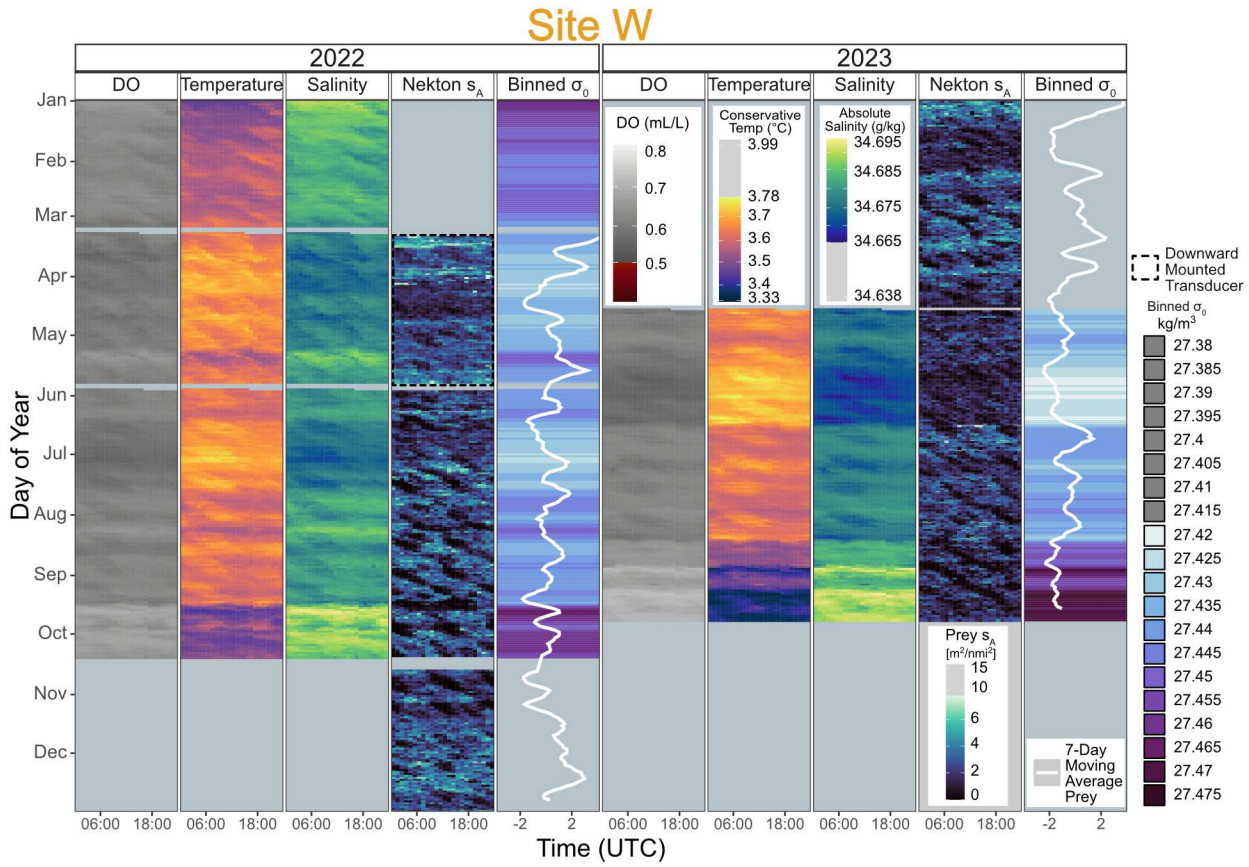

Fig. 2 — Multi-scale temporal variability in hydrography and nekton backscatter at Site W. Hourly-binned mooring observations for 2022 (left panels) and 2023 (right panels), plotted by day of year (y-axis) and time of day in UTC (x-axis). Conservative temperature (Θ; °C, labeled as temperature), absolute salinity (S_A; g kg^{-1}, labeled as salinity), and DO (mL L^{-1}) were recorded by MicroCAT instruments at depths >1000 m. Hourly-binned nekton s_A (m^2 nmi^{-2}) is summed across the sampled range. To highlight variability at weekly to monthly timescales, a normalized 7-day moving average of daily s_A is overlaid as a white line on daily average σ_0 (kg m^{-3}) binned into 0.005 kg m^{-3} intervals. Color scales are site-specific and follow perceptually uniform oceanographic color conventions [78]; grayed portions of each color bar indicate values observed elsewhere in the full dataset but absent at Site W. Gray panels indicate periods with no data. A dashed rectangle denotes the period during which the acoustic transducer was downward-mounted.

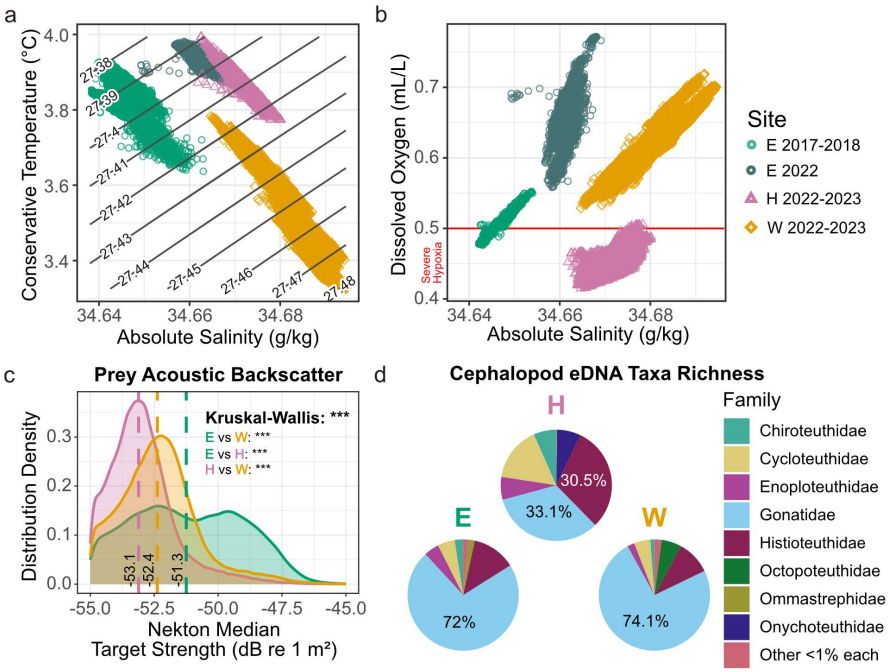

Fig. 3 — Hydrographic conditions and nekton community structure across Southern California Bight submarine basin sites. (a) Θ (°C) versus S_A (g kg^{-1}) for h-averaged MicroCAT data ($n = 38{,}191$ observations across all sites) at Sites W (orange diamonds), H (pink triangles), and E (light green circles: 2017–2018; dark green circles: 2022) at depths >1000 m. Isopycnals of σ_0 (kg m^{-3}) are shown as diagonal gray lines. **(b)** DO (mL L^{-1}) versus S_A (g kg^{-1}) for the same observations. The horizontal red dashed line indicates the severe hypoxia threshold (DO $\leq$ 0.5 mL L^{-1}) [40]. **(c)** Distributions of nekton median TS (dB re 1 m^2) for individual single-target tracks at Sites E (n = 56,821), W (n = 181,292), and H (n = 116,611). Vertical dashed lines indicate site-specific median TS values (E: −51.3 dB re 1 m^2, W: −52.4 dB re 1 m^2, H: −53.1 dB re 1 m^2). Differences among sites were tested using a Kruskal-Wallis test followed by pairwise Wilcoxon rank-sum tests with Benjamini-Hochberg correction (*** = $p < 0.001$). **(d)** Family-level cephalopod eDNA composition from CTD-cast samples collected below 500 m at Sites E and H ($n = 2$ casts each) and W ($n = 3$ casts). Dominant families are labeled by percentage contribution; families each comprising <1% of detections are grouped as "other".

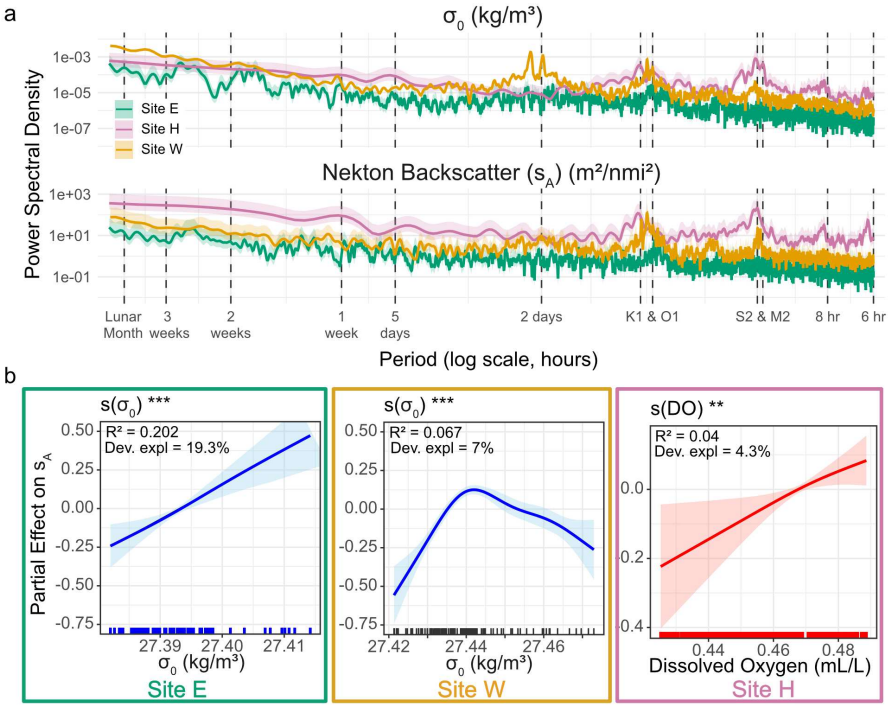

Fig. 4 — Spectral periodicity and environmental predictors of nekton backscatter across sites. **(a)** Smoothed spectral density estimates (Welch-type periodograms with modified Daniell spans (5, 5) and 10% cosine taper) of σ_0 (kg m^{-3}) and s_A (m^2 nmi^{-2}) at Sites E (green), W (orange), and H (pink), plotted on a log-scaled period axis. Shaded ribbons indicate 95% confidence intervals derived from the chi-squared distribution. Vertical dashed lines indicate known tidal constituents (S2, M2, K1, O1) and other ecologically relevant periodicities. **(b)** Site-specific GAM partial effects (centered smooth terms) of the dominant environmental predictor on s_A: σ_0 (kg m^{-3}) at Sites E (green border) and W (orange border), and DO (mL L^{-1}) at Site H (pink border). Shaded ribbons indicate 95% confidence intervals; rug marks along the x-axis show the distribution of observations. Model fit statistics (R^2 and deviance explained) are shown for each panel. Y-axis values are centered smooth terms and are not comparable in absolute magnitude among panels.

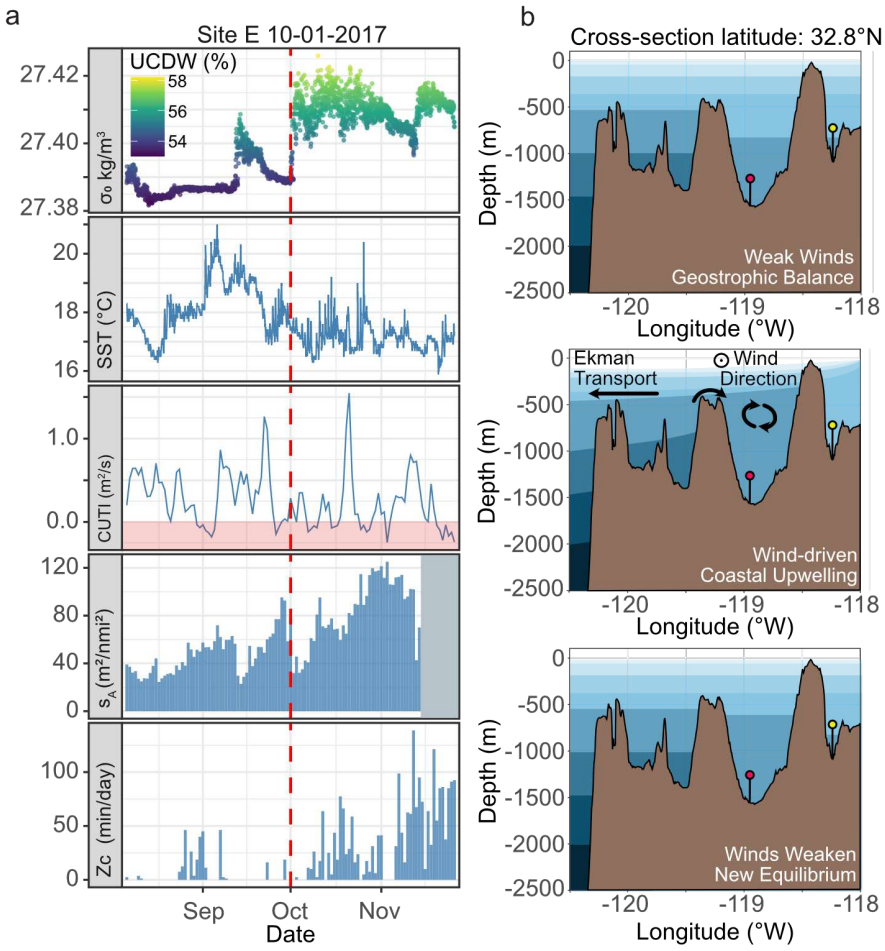

Fig. 5 — Basin flushing event at Site E and proposed ventilation mechanism. **(a)** Time series spanning 8 weeks before and after the October 2017 flushing event (vertical red dashed line) at Site E. From top to bottom: h-averaged σ_0 (kg m^{-3}) colored by UCDW fraction (%); 6-h SST (°C) from NOAA buoy Station 46219 [50]; daily CUTI at 33°N [42] (pink shading indicates downwelling conditions, CUTI < 0); daily s_A (m^2 nmi^{-2}); and daily *Z. cavirostris* acoustic presence (min day^{-1}). Analogous time series for flushing events at Site W are shown in Extended Data Fig. 4. **(b)** Conceptual cross-sections at 32.8°N illustrating the proposed flushing mechanism under three sequential conditions: geostrophic balance with weak winds (top); wind-driven coastal upwelling with offshore Ekman transport and isopycnal shoaling toward basin sill depths (middle); and post-relaxation equilibrium in which denser UCDW has intruded into adjacent basins at depth (bottom). Filled red and yellow circles indicate the approximate locations of Sites E and H.

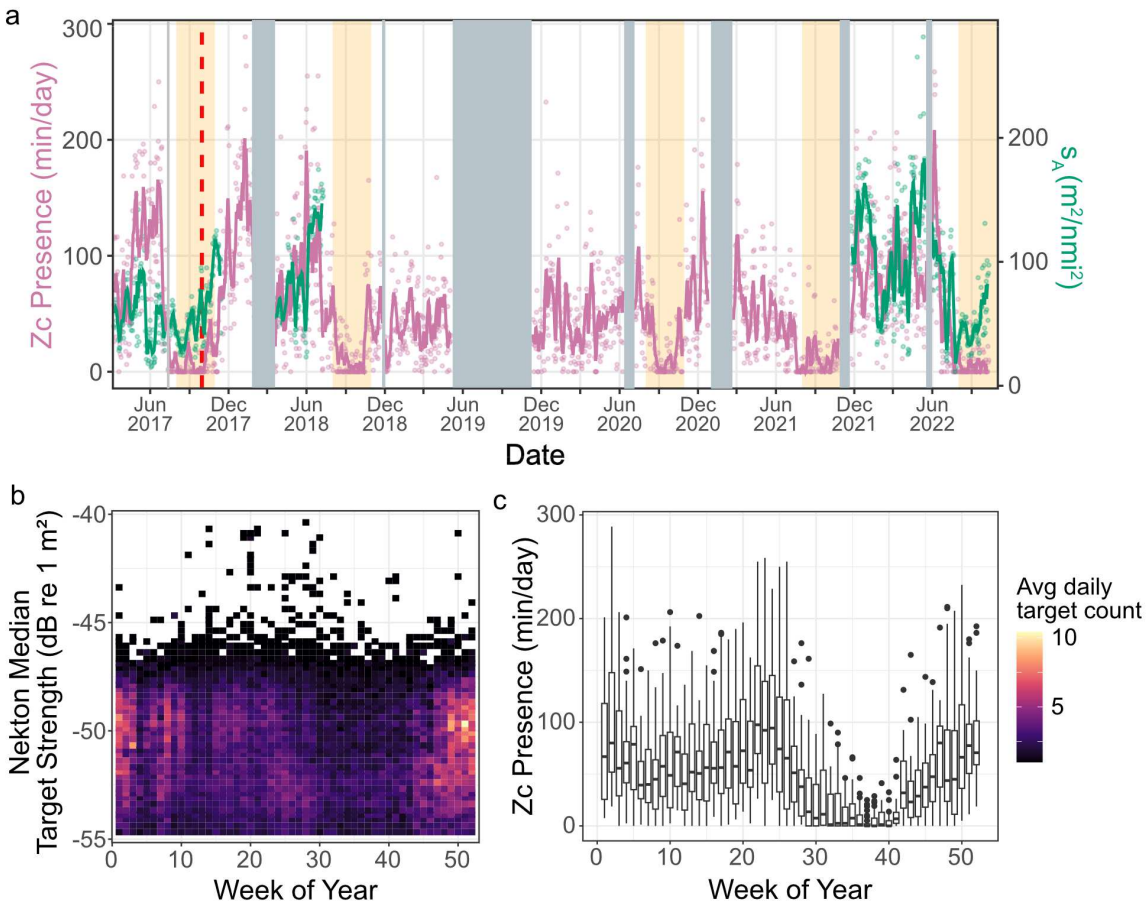

Fig. 6 — Seasonal and interannual coupling of *Z. cavirostris* acoustic presence and nekton backscatter at Site E. (a) Daily *Z. cavirostris* acoustic presence (min day^{-1}; pink circles) and s_A (m^2 nmi^{-2}; green circles) at Site E from 2017–2022, with 7-day moving averages overlaid as solid lines. Yellow shading indicates the late-summer *Z. cavirostris* minimum (weeks 31–44; August–October). Gray shading indicates periods with no data. The vertical red dashed line marks the October 2017 flushing event. **(b)** Heat map of nekton median *TS* (dB re 1 m^2) by week of year at Site E, restricted to the −55 to −40 dB re 1 m^2 *TS* range; color indicates mean daily single-target count in 0.25 dB *TS* bins. **(c)** Weekly box plots of *Z. cavirostris* acoustic presence (min day^{-1}) aggregated across all available years at Site E. Boxes show the interquartile range; horizontal lines show the median; whiskers extend to 1.5× the interquartile range; filled circles show outliers.

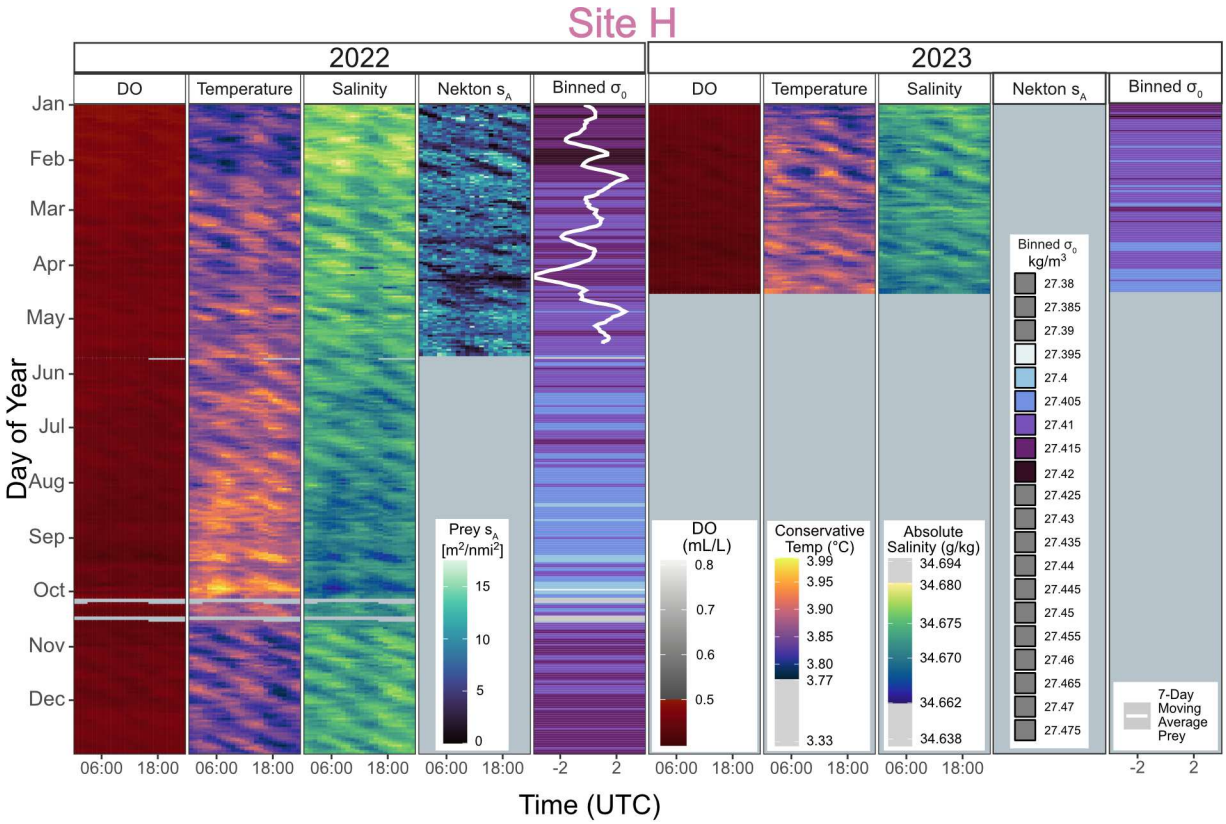

Extended Data Fig. 1 – Multi-scale temporal variability in hydrography and nekton backscatter at Site H. Hourly-binned mooring observations for 2022 (left panels) and 2023 (right panels), plotted by day of year (y-axis) and time of day in UTC (x-axis). Conservative temperature (Θ; °C, labeled as temperature), absolute salinity (S_A; g kg^{-1}, labeled as salinity), and DO (mL L^{-1}) were recorded at depths >1000 m. Hourly-binned nekton s_A (m^2 nmi^{-2}) is summed across the sampled range; gray panels indicate periods with no data. To highlight variability at weekly to monthly timescales, a normalized 7-day moving average of daily s_A is overlaid as a white line on daily average σ_0 (kg m^{-3}) binned into 0.005 kg m^{-3} intervals. Color scales are site-specific and follow perceptually uniform oceanographic color conventions [78]; grayed portions of each color bar indicate values observed elsewhere in the full dataset but absent at Site H.

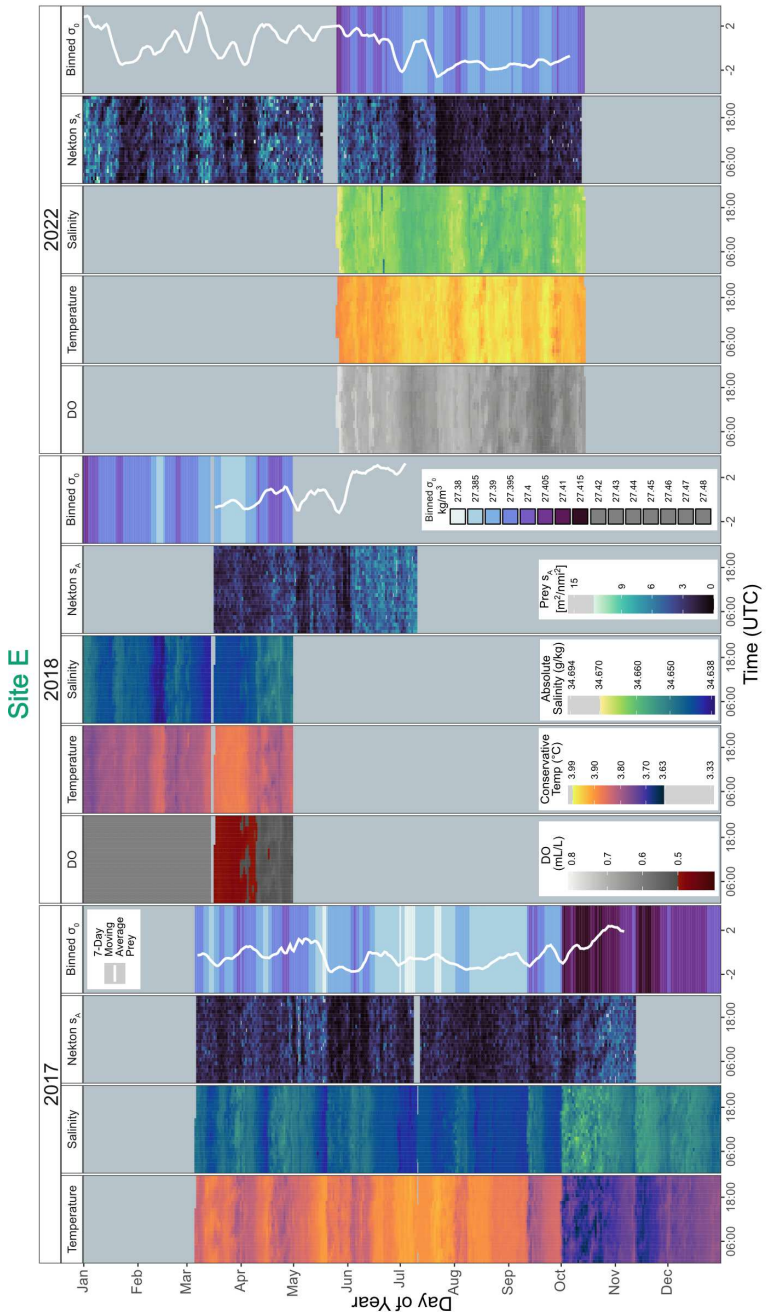

Extended Data Fig. 2 – Multi-scale temporal variability in hydrography and nekton backscatter at Site E. Hourly-binned mooring observations for 2017 (left panels) and 2018 (right panels), plotted by day of year (y-axis) and time of day in UTC (x-axis). Conservative temperature (Θ; °C, labeled as temperature), absolute salinity (S_A; g kg^{-1}, labeled as salinity), and DO (mL L^{-1}) were recorded at depths >1000 m (see Table S1).Hourly-binned nekton s_A (m^2 nmi^{-2}) is summed across the sampled range. To highlight variability at weekly to monthly timescales, a normalized 7-day moving average of daily s_A is overlaid as a white line on daily average σ_0 (kg m^{-3}) binned into 0.005 kg m^{-3} intervals. Color scales are site-specific and follow perceptually uniform oceanographic color conventions [78]; grayed portions of each color bar indicate values observed elsewhere in the full dataset but absent at Site E. Gray panels indicate periods with no data. The 2018 salinity record includes a corrected deployment offset (see Methods).

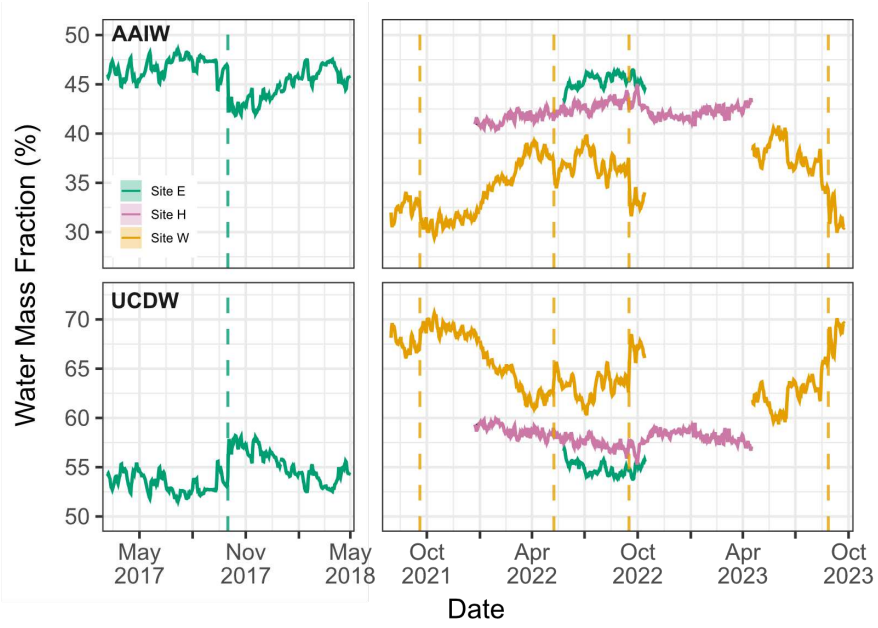

Extended Data Fig. 3 – Water mass fractions estimated from OMP analysis. Time series of AAIW (top row) and UCDW (bottom row) fractions expressed as percentages of the three-endmember mixture at Sites E (teal), H (pink), and W (orange). Left column shows Site E observations from the 2017–2018 deployments; right column shows Site E, H and W from 2021–2023. Endmember properties used in the OMP decomposition are given in Table S6. Dashed vertical lines mark identified flushing events (Table S4) with color indicating site.

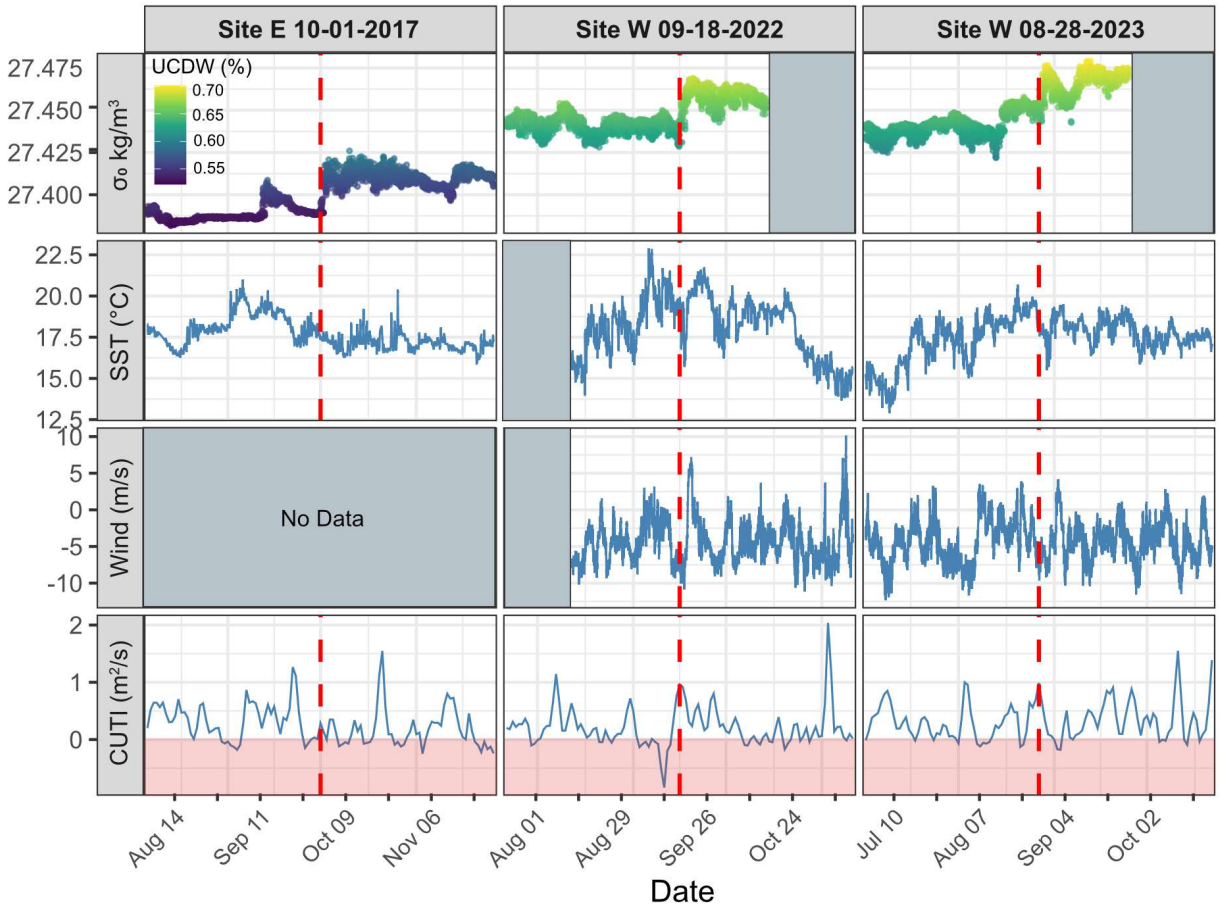

Extended Data Fig. 4 – Atmospheric and surface ocean conditions surrounding identified flushing events. Each column shows a 12-week window centered on a flushing event (red dashed line) at Site E on 10 October 2017 (left), Site W on 18 September 2022 (center), and Site W on 28 August 2023 (right). Top row: σ_0 (kg m^{-3}) calculated from measurements at depth and colored by UCDW fraction (%) from OMP analysis. Second row: SST (°C) from the nearest NOAA National Data Buoy Center buoy [50]. Third row: meridional wind speed (m s^{-1}) at the nearest NOAA National Data Buoy Center buoy [50]; positive values indicate northward (downwelling-favorable) winds; no wind data were available for the 2017 event. Bottom row: daily CUTI at 33°N [42]; pink shading indicates downwelling conditions (CUTI < 0).

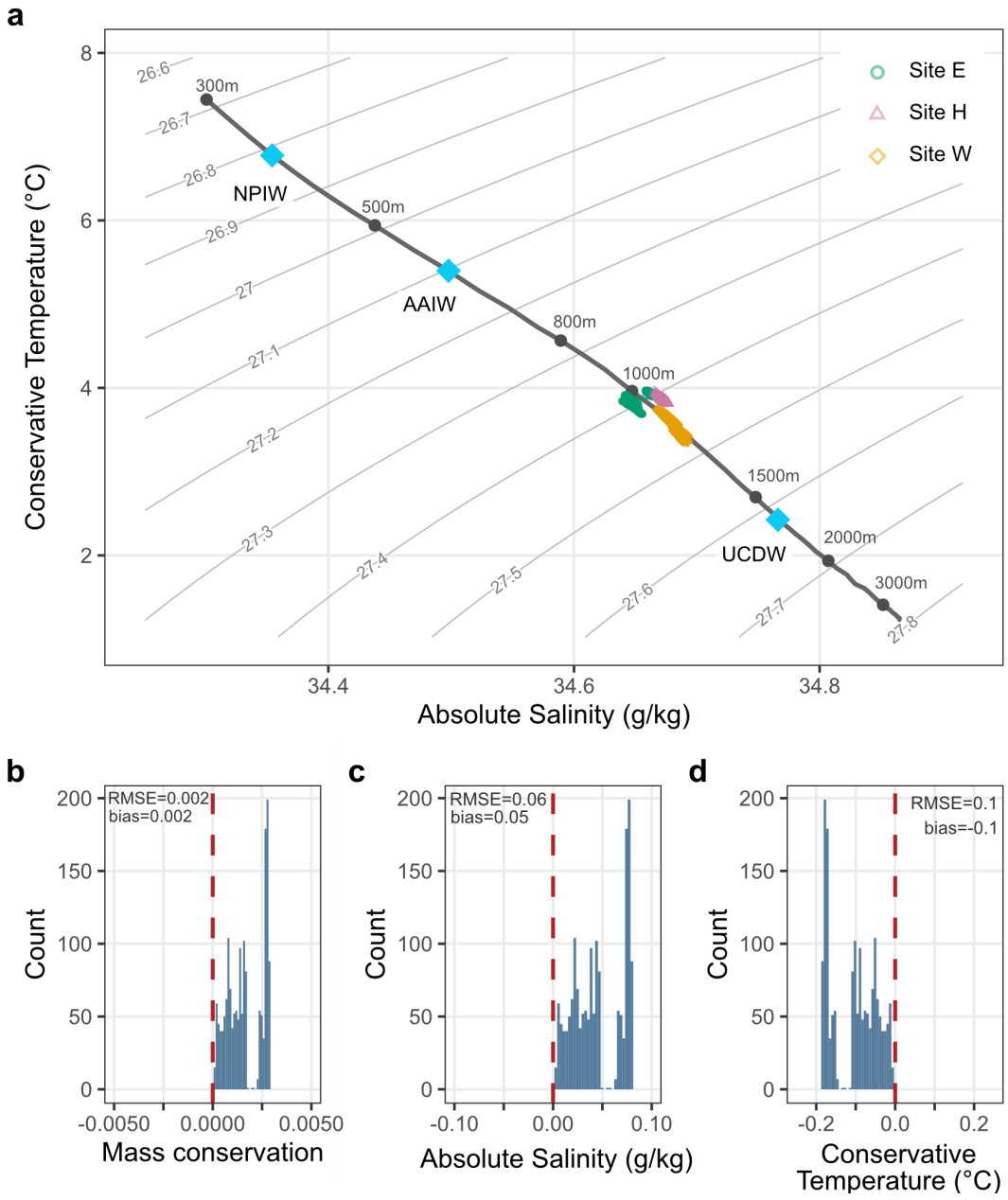

Extended Data Fig. 5 – OMP analysis end-member placement and residual diagnostics. (a), Temperature–salinity diagram showing the WOA23 annual climatological profile at 33°N, 120°W (grey curve) [48, 49] selected depth levels indicated (filled grey circles). End members used in the OMP analysis (cyan diamonds) are shown at their characteristic isopycnal surfaces: NPIW ($\sigma_0 \approx 26.8$), AAIW ($\sigma_0 \approx 27.1$), and UCDW ($\sigma_0 \approx 27.6$). Daily-averaged observations from Sites E (teal), H (pink), and W (orange) cluster along the WOA23 climatological curve in the AAIW–UCDW mixing region, consistent with mooring depths of ∼1200 m. **b–d**, Histograms of OMP residuals for mass conservation **(b)**, S_A **(c)**, and Θ **(d)**. Dashed red lines indicate zero residual.

Supplementary Files

This is a list of supplementary files associated with this preprint. Click to download.

- DolanetalBasinFlushingNektonSupplementary.pdf